HHS Public Access

Author manuscript

Neuroscience. Author manuscript; available in PMC 2022 October 15.

Published in final edited form as:

Neuroscience. 2021 October 15; 474: 63–79. doi:10.1016/j.neuroscience.2020.11.014.

Glymphatic Cerebrospinal fluid and solute transport quantified by MRI and PET imaging

Helene Benveniste[1,2], **Hedok Lee**[1], **Burhan Ozturk**[1], **Xinan Chen**[3], **Sunil Koundal**[1], **Paul Vaska**[4], **Allen Tannenbaum**[3], **Nora D. Volkow**[5]

[1]Department of Anesthesiology, Yale School of Medicine, New Haven, CT

[2]Department of Biomedical Engineering, Yale School of Medicine, New Haven CT

[3]Departments of Computer Science and Applied Mathematics & Statistics, Stony Brook University, Stony Brook NY

[4]Department of Radiology, Stony Brook University, Stony Brook, NY

[5]Laboratory for Neuroimaging, NIAAA, Bethesda, MD

Abstract

Over the past decade there has been an enormous progress in our understanding of fluid and solute transport in the central nervous system (CNS). This is due to a number of factors, including important developments in whole brain imaging technology and computational fluid dynamics analysis employed for the elucidation of glymphatic transport function in the live animal and human brain. In this paper, we review the technical aspects of dynamic contrast enhanced magnetic resonance imaging (DCE-MRI) in combination with administration of Gd-based tracers into the cerebrospinal fluid (CSF) for tracking glymphatic solute and fluid transport in the CNS as well as lymphatic drainage. Used in conjunction with advanced computational processing methods including optimal mass transport analysis, one gains new insights into the biophysical forces governing solute transport in the CNS which leads to intriguing new research directions. Considering drainage pathways, we review the novel T1 mapping technique for quantifying glymphatic transport and cervical lymph node drainage concurrently in the same subject. We provide an overview of knowledge gleaned from DCE-MRI studies of glymphatic transport and meningeal lymphatic drainage. Finally, we introduce positron emission tomography (PET) and CSF administration of radiotracers as an alternative method to explore other pharmacokinetic aspects of CSF transport into brain parenchyma as well as efflux pathways.

Helene Benveniste, M.D., Ph.D., Professor of Anesthesiology, Department of Anesthesiology, Yale School of Medicine, 333 Cedar Street/TMP3, New Haven, CT 06510, 203-737-1516, Helene.benveniste@yale.edu.

Conflicts of interest: None

Financial disclosures: NIH R01AG048769, RF1 AG053991, R01AG057705 and Leducq Foundation (16/CVD/05)

Background

This review focuses on technical aspects and new knowledge of fluid and solute transport via the glymphatic system and connected drainage pathways gained over the last decade using magnetic resonance imaging (MRI) and positron emission tomography (PET). However, a brief historical overview on cerebrospinal fluid (CSF) transport research is appropriate given the considerable knowledge gained from these now classical studies. Roy Mott (Mott, 1910) and Weed (Weed, 1922) were among the earliest anatomists to conceptualize and describe CSF flow via peri-vascular conduits in the central nervous system (CNS). In Weed's book on CSF, the peri-vascular fluid channels were referred to as 'lymphatic' in character (Weed, 1922). Weed (Weed, 1922) and Halliburton (Halliburton, 1917) further documented that the perivascular fluid channels acted as communication routes between subarachnoid fluid and interstitial fluid (ISF) of neuropil. Importantly, Weed highlighted that 'in comparison to blood flow, velocities of the CSF are slow and more difficult to measure" (Weed, 1922). Several decades later, Weller described the Virchow-Robin spaces around the large arteries as they enter the normal human brain and their complex leptomeningeal sheaths and connections to the subarachnoid space (Weller et al., 1992). He further emphasized that the perivascular space for CSF passage along the penetrating arteries became virtual conduits comprising only the basement membrane at the level of the capillary bed (Weller, et al., 1992). In 1985, Rennels and coworkers pioneered new dynamic information on rapid brain-wide perivascular solute movement (Rennels et al., 1985). They infused horseradish peroxidase into CSF via the lateral ventricle or cisterna magna of the cat brain and noted rapid (~4min) distribution of the tracer surrounding all penetrating arterioles across brain structures (Rennels, et al., 1985). Notably, they also showed that arterial pulsations were required for the rapid perivascular solute flow (Rennels, et al., 1985). Several reviews on CSF flow and CNS homeostasis are available and the interested reader is referred to these for more detail (Abbott et al., 2018, Hladky and Barrand, 2014, Johnston, 2003, Louveau et al., 2015, Louveau et al., 2017, Raper et al., 2016). Fast-forwarding to 2012, Iliff and Nedergaard introduced the glymphatic system as a brain-wide perivascular transit passageway for CSF facilitating waste clearance from the brain in a manner dependent on glial cells and aquaporin 4 (AQP4) water channels (Iliff et al., 2012, Mestre et al., 2018).

Waste and solute drainage via the glymphatic system have been studied extensively in the live rodent brain (Ding et al., 2018, Gaberel et al., 2014, Huber et al., 2018, Iliff et al., 2014, Lee et al., 2015, Morris et al., 2016, Yang et al., 2013), non-human primate brain (Goulay et al., 2018, Ohno et al., 2019), and human brain (Eide and Ringstad, 2015, Eide and Ringstad, 2018, Ringstad et al., 2017), and is conceptualized as a dynamic 3-step process: (1) bulk-flow driven influx of CSF from the peri-arterial compartment into interstitial fluid (ISF); (2) CSF-ISF mixing in the neuropil driving extracellular waste solutes towards peri-venous conduits; and (3) exit of waste solutes from peri-venous conduits into lymphatic vessels with subsequent systemic absorption and metabolic breakdown (Iliff, et al., 2012). The working hypothesis of solute and fluid transport through the glymphatic system is still under investigation, in particular, the issue of direction and biophysical forces underlying solute flow in neuropil. The current controversies pertaining to glymphatic

transport and solute movement in CSF and neuropil can be researched in several reviews and the interested reader is referred to these for more information (Abbott, et al., 2018, Benveniste et al., 2019, Brinker et al., 2014, Mestre et al., 2020, Wardlaw et al., 2020). In regards to characterization and further understanding of the lymphatic exit pathways this has been accomplished by the creation of lymphatic endothelial cell-specific fluorescent reporter mice and immunofluorescent staining for lymphatics such as LYVE-1, PROX-1 and VEGFR-3 (Truman et al., 2013). Thus, an intricate but rather sparse network of bona fide lymphatic vessels in the dura mater of the brain was uncovered (Aspelund et al., 2015, Louveau et al., 2015) and spinal cord (Antila et al., 2017, Jacob et al., 2019) and shown to drain specific anatomical districts of lymph nodes (Antila, et al., 2017, Da Mesquita et al., 2018, Jacob, et al., 2019, Louveau et al., 2018, Louveau, et al., 2015).

Glymphatic system transport captured *in vivo* by dynamic contrast enhanced MRI

The need to capture brain-wide glymphatic solute transport in real time was essential to further define transport kinetics and for exploring the physiological drivers of the system. Although, post-mortem approaches provided proof of peri-arterial influx of small molecular weight (MW) tracers from CSF into ISF, the unavoidable tissue processing including formalin-fixation affected uptake patterns and therefore data interpretation (Mestre et al., 2018). For example, from the first glymphatic system study it was shown that small molecular weight (MW) fluorescently tagged tracers like Texas-red distributed very rapidly (~30min after CSF administration) from CSF into ISF across the whole brain (Iliff, et al., 2012). It has now been repeatedly shown by *in vivo* imaging (vide infra) that extracellular tracer distribution from CSF into all regions of the brain is rather slow because glymphatic transport kinetics across brain regions is heterogeneous (Iliff et al., 2013, Lee, et al., 2015).

MRI which is an inherently three-dimensional (3D) and non-invasive technique was an obvious first choice for exploring glymphatic system transport dynamics in the live rodent brain (Iliff, et al., 2013). Spatial resolution and endogenous tissue contrast of MRI images acquired at high magnetic field was excellent for visualizing brain anatomy and larger vascular structures necessary for interpreting glymphatic system fluid and solute fluxes across compartments. Specifically, dynamic contrast enhanced MRI (DCE-MRI) using a 3D T1-weighted pulse sequence, in combination with CSF administration of paramagnetic contrast molecules was used for visualizing glymphatic system transport in the whole rat brain (Iliff, et al., 2013). Given the reported slower velocity ranges of CSF flow when compared to blood flow (Haughton et al., 2003), the temporal resolution of DCE-MRI was also suitable to capture macro- and mesoscale biophysical kinetic patterns of glymphatic solute transport (Lee, et al., 2015, Mortensen et al., 2019). In the first study of glymphatic transport in rat brain by DCE-MRI, the rat with the indwelling CSF catheter in the cisterna manga (Fig. 1A) was placed supine with the small RF surface coils positioned underneath the head (Fig. 1B). In two different series of rats, gadopentetate dimeglumine (Gd-DTPA, MW 938 Da) or the larger MW polymeric Gd-chelate GadoSpin (200,000 Da) was administered into the CSF via a small catheter implanted into the cisterna magna of rats anesthetized with a long-acting barbiturate (Iliff, et al., 2013). The small and large

MW paramagnetic contrast molecules were used to validate the previously reported presence of bulk flow along the peri-arterial CSF influx routes (Iliff, et al., 2012, Rennels, et al., 1985). If peri-arterial transport is driven by bulk flow, solute speed would be independent of the contrast molecule's MW. To compare glymphatic transport between Gd-DTPA and GadoSpin their respective T1 relaxation effects had to be matched and 0.17 mM GadoSpin and 21 mM Gd-DTPA solutions were determined to fulfill these requirements (Iliff, et al., 2013). We note that a large volume of the paramagnetic contrast solute was delivered intrathecally (80 μl at a rate of 1.6 μl/min) with the goal of 'saturating' and achieving sufficient contrast enhancement in all brain regions. The DCE-MRI data was acquired using a dynamic 3D T1-weighted FLASH sequence acquired over ~4.2 hrs. To visualize glymphatic transport of the tracer, the DCE-MRI data were converted into parametric maps in which the signal intensity of each voxel represented 'percentage signal change from the baseline' also referred to as the 'enhancement ratio' (Iliff, et al., 2013). Fig. 1 shows whole brain glymphatic uptake patterns of Gd-DTPA (Figs. 1C–E) and GadoSpin (Figs. 1F–H) ~90 min following contrast administration. Glymphatic transport is presented as a 3D volume rendered color-coded map overlaid on the corresponding anatomical template of the rat brain. It is evident that there is more tissue uptake of Gd-DTPA in comparison to GadoSpin. Parenchymal uptake of Gd-DTPA is extensive especially in the cerebellum and along ventral surface (brainstem, pons, hypothalamus), ventral hippocampus, and olfactory bulb (Figs. 1C–E). GadoSpin with a MW of 200,000 Da has restricted access from the perivascular space via the astrocytic end-feet gaps (~20–30nM) to ISF, and it therefore accumulates in the subarachnoid CSF and the perivascular space of the larger pial surface arteries as well as along dural sinuses (Figs. 1F–H). Several investigators have reproduced this characteristic spatial distribution pattern of glymphatic transport with different paramagnetic agents in a wide variety of animal species including human brain using DCE-MRI (Table 1). In the following sections we will highlight key technical features that have been refined over time. Further, the parametric quantitative output of solute and fluid transport as well as new knowledge of glymphatic system function revealed by DCE-MRI is presented in Table 2.

CSF infusion rate, total Gd contrast mass and volume for glymphatic transport by MRI

When performing glymphatic studies using DCE-MRI and Gd-based contrast administration into CSF it is important that the intracranial pressure (ICP) remains within normal limits during the experiment. A higher than normal ICP will affect cerebral blood flow and if severely elevated will compromise tissue perfusion, induce ischemia leading to cytotoxic edema and decreases in the ISF volume fraction which will adversely impact glymphatic transport (Mestre et al., 2020). Conversely, a lower than normal ICP can emerge if CSF is leaking during the cisterna magna cannulation (or deliberately via cisternotomy (Plog et al., 2015)) or if the experiment is conducted in the setting of an open, unsealed craniotomy with dura removed. Regardless, any alteration of ICP from normal levels will change intracranial hydraulic pressure gradients and impact glymphatic transport dynamics. Table 1 shows that the total Gd-based contrast volume used in glymphatic studies are generally adjusted to the physical size of the CSF compartment of the species to avoid excessive ICP changes. For example, the CSF compartment volume determined by anatomical MRI in normal rat and

mouse is ~250μl (Lee et al., 2020) and ~40μl (Ma et al., 2008), respectively. Further, the CSF production rate in adult mice is ~0.35μl/min (Pardridge, 2016) and ~1.5μl/min in young adult rats (Karimy et al., 2015). Considering these numbers, Gd-contrast volumes in the range of ~20–30 μl infused at rates of 0.5–3μl/min (Ding, et al., 2018) used in glymphatic rat studies are physiologically reasonable and associated with only minor transient increases in ICP (Koundal et al., 2020). Similarly, for mice, Gd-contrast volumes in the range of 1–10μl using infusion rates of ~1–2μl/min are regarded to be safe and associated with minor, transient increases in ICP (Xue et al., 2020). However, these recommendations are based on experiments conducted in spontaneously breathing rodents anesthetized with a wide variety of hypnotic and anesthetic agents, which affect ICP differently and thus CSF infusion conditions. Several studies listed in Table 1 have recorded only subtle elevations of ICP during the CSF infusion and it is therefore inferred that unphysiological ICP conditions did not impact glymphatic transport dynamics.

Differences across DCE-MRI studies in regard to Gd-contrast concentration and total ‘mass’ delivered into CSF (Table 1) is a tradeoff between achieving sufficient Gd-contrast uptake in the whole brain for detection by T1-weighted MR contrast (T1 shortening) while not ‘overshooting’ the local Gd tissue concentration, which would induce unwanted susceptibility T2* and signal loss (Lee et al., 2018). Another issue to consider in DCE-MRI studies is the baricity of the Gd-contrast mixture administered into CSF. Baricity is the ratio of the density of a local anesthetic solution to the density of CSF. Density is defined as the mass per unit volume of solution (g/mL) and the density of CSF is 1.0004–1.0006 g/L. If the Gd-contrast mixture has the same density as CSF it is ‘isobaric’, and those with higher and lower density than CSF are hyperbaric and hypobaric, respectively. A commonly used Gd-based molecule for glymphatic studies is the commercially available gadoterate meglumine delivered as an aqueous 500mM solution (Dotarem®, Gerbet LLC, France). In the manufacturer’s formulation, the density of Dotarem (a.k.a. Gd-DOTA) is given as 1.1753 g/ml and the osmolarity as 1350 mOsm/kg water (Agency). Thus, administering Gd-DOTA in a concentrated formulation which is hyperbaric as well as hyperosmotic compared to CSF (osmolarity of normal CSF ~285–290 mOsm/kg) might influence the distribution pattern and transport kinetics assessed via the glymphatic system. Currently there is a gap in knowledge as to how baricity and osmotic pressure of the contrast/tracer solutions affect glymphatic transport data and more studies are needed to clarify these issues. Fig. 2 shows an example of a glymphatic DCE-MRI study with CSF Gd-DOTA administered in a 1:5 dilution in combination with a small RF surface coil positioned over the left hemisphere of an anesthetized rat (Koundal, et al., 2020). These technical implementations were done specifically to increase perivascular Gd-contrast enhancement along the middle cerebral artery and enabled documentation of perivascular solute and fluid transport impairment in a rat model of chronic hypertension (Koundal, et al., 2020).

Glymphatic transport and body posture

For glymphatic transport experiments it is important to track physiological parameters carefully including stability of the anesthetic state. Most glymphatic transport studies are carried out in anesthetized, spontaneously breathing rodents positioned either supine or prone with the head fixed in a stereotaxic frame or head holder (so-called sphinx position).

The body position used for glymphatic transport experiments in rodents is important because each head/body position (e.g. supine, prone, or lateral recumbent) are associated with diverse changes in several physiological parameters including ICP, central venous pressure and heart rate. We previously investigated the effect of body position on glymphatic transport in anesthetized rodents (Lee, et al., 2015). Our study showed that the prone sphinx position with the head above the heart decreased glymphatic transport and clearance of soluble Aβ in comparison from the neuropil in comparison to supine and lateral recumbent body positions (Lee, et al., 2015). Thus, in the sleeping or anesthetized state where the glymphatic system is vigorously engaged in solute and fluid transport (when compared to wakefulness) (Xie et al., 2013) the most beneficial sleeping positions from the point of view of waste clearance would be supine and/or lateral recumbent body positions. Interestingly, studies have shown that the right lateral sleeping position is the most favored by adult humans (De Koninck et al., 1992). According to reports from veterinarians and wild-life scientists, rodents sleep ‘naturally’ in groups with other rats to bond and share warmth and this can include a wide range of body postures. However, in experimental settings or single caged housing, rodents’ sleeping positions are lateral, ‘curled up’ with the head tucked in towards the legs. Ideally, glymphatic studies should be carried out in the most physiological correct conditions, and lateral recumbent body posture with the head gently bent might be more ‘natural’ when compared to supine body position. However, in many experimental setting including MRI imaging with physiological monitoring and indwelling CSF catheters this may be difficult to mimic the ‘natural’ sleeping position of the given species studied; and this should be considered with interpreting glymphatic transport data.

T1 mapping technique for quantifying glymphatic and lymphatic transport

In glymphatic studies, the enhancement ratio (ER) defined as % signal change from the baseline is a semi-quantitative technique that is simple to calculate and easy to interpret because in normal brain tissue, ER values are proportional to the Gd concentration (Benveniste et al., 2017, Harrison et al., 2020, Lee, et al., 2018, Lee, et al., 2015). However, ER data obtained in neurodegenerative disease states should be interpreted with care because pathophysiological conditions (e.g. stroke, hemorrhage or brain injury) alters the tissue T1 when compared to normal healthy tissue (Barbier et al., 2005). When the pre-contrast T1 of the pathological tissue is significantly different from normal values, the relationship between the ER and Gd concentration also changes and this can lead to inaccurate conclusions. For example, if the T1 is different between normal and pathological tissue the ER may erroneously reflect this difference but in fact the Gd concentration (and glymphatic solute transport) might remain unchanged. To circumvent this problem, and to derive accurate glymphatic solute transport measures it is necessary to calculate the actual Gd concentration (mM) instead of using the ER. To this end, we developed a 3D T1 mapping technique using 3D variable flip angle spoiled gradient echo sequence (VFA-SPGR) and processing algorithms for converting ER to Gd concentrations (Lee, et al., 2018, Mortensen, et al., 2019). The VFA-SPGR protocol comprises acquisition of SPGR images at multiple flip angles and the protocol can be implemented easily since it does not require specialized hardware or pulse sequences. However, it is well known that T1 derived from VFA-SPGR data can be inaccurate in the presence of substantial RF transmit coil inhomogeneity (B1+)

resulting in spatially heterogeneous flip angle, which deviate from the nominal flip angle. Therefore B1+ correction is essential for calculating accurate VFA-SPGR T1 maps (Lee, et al., 2018). Using T1 mapping wtih Gd concentration calculations we previously estimated that only ~20% of Gd contrast was transported into the brain from the CSF (cisterna magna) inferring that the bulk of tracer mass does not enter the brain-wide glymphatic system but migrate to spine and or drains directly to the lymphatics (Lee, et al., 2018, Lee, et al., 2015, Xue, et al., 2020).

The T1 mapping technique is also advantageous for quantifying glymphatic transport as well as drainage of the Gd contrast solute to the cervical lymph nodes (superficial as well as deep cervical lymph nodes) *in vivo* (Xue, et al., 2020). Fig. 3 shows the T1 mapping approach for quantifying glymphatic transport and cervical lymphatic drainage in a mouse anesthetized with ketamine/xylazine. With this particular technique, the Gd-DOTA is administered on the bench, and the CSF catheter is removed after the injection prior to MRI scanning which, makes the set up less technically challenging and more time efficient (Xue, et al., 2020). The first T1 map is acquired approximately 1 hr after the administration of contrast and represents a single ‘snapshot’ of glymphatic transport and lymphatic drainage at this time point (Xue, et al., 2020). The field-of-view of the T1 maps includes the head and neck of the mouse so glymphatic Gd-DOTA and drainage of Gd-DOTA to the cervical lymph nodes can be quantified in the same mouse (Fig. 3). The superficial (submandibular) cervical lymph nodes are located rostral to the submandibular gland (Figs. 3A, B) while the deep cervical lymph nodes are located lateral and posterior to the trachea and common carotid arteries (Figs. 3C, D). The cervical lymph nodes appear ‘dark’ after Gd-DOTA drainage because of T1 shortening which lowers the T1 by ~30–205% when compared to normal T1 tissue values (Figs. 3E, F). The glymphatic transport and drainage of Gd-DOTA to the cervical lymph nodes are quantified by measuring the number voxels of T1 values at a specific range (e.g. 1–1800 ms) and this volume can then be compared to control mice (normal T1 values ~2000ms) (Xue, et al., 2020). A similar approach can be used in human DCE-MRI studies though parenchymal uptake and clearance of contrast requires days rather than hours and data must be collected over multiple visits (Ringstad, et al., 2017, Watts et al., 2019).

Quantification of glymphatic transport from DCE-MRI data

In order to interpret DCE-MRI glymphatic studies and how this technology have contributed to knowledge on the system’s function in normal and diseased brain it is important to briefly discuss how solute and fluid transport is quantified. In the following we will discuss glymphatic system transport quantification by K-means cluster analysis, kinetic tissue compartment modeling and optimal mass transport processing.

K-means cluster analysis:

Glymphatic influx of the Gd-based contrast solute into brain was originally quantified across regions and in whole brain using ‘time-signal’ curves (time-to-peak and ‘area under curve time-integrals) as well as k-means cluster analysis (Iliff, et al., 2013). Fig. 4 shows an example of k-means 3-cluster analysis using a DCE-MRI glymphatic study with CSF Gd-DOTA administration from a normal 3M old Sprague Dawley rat. The 3 tissue

compartments defined by k-means cluster analysis are shown as binary volume rendered color-coded masks overlaid on the corresponding anatomical brain (Figs. 4B–D). While the red cluster is located in the CSF compartment proper and includes the basal cisterns (Fig. 4B) the blue cluster is 'parenchymal' (Fig 4D). The green cluster represents an mixed cluster comprising subarachnoid CSF, CSF in the peri-vascular compartments of large arteries as well as adjacent tissue (Fig. 4C). The corresponding time signal curves (TSC) from the three clusters are shown in Fig. 4E. The red cluster's TSC represents the smallest tissue compartment (2487 voxels) and is characterized by high peak magnitude (~300% signal increase) and rapid decay (Fig. 4E). The parenchymal TSC represents the largest tissue volume (10015 voxels) and is characterized by low signal magnitude and slow decay (Fig. 4D). More details and further development of the cluster analysis approach for glymphatic system transport analysis can be found in Davoodi-Bojd et al. (Davoodi-Bojd et al., 2019).

Tissue compartment kinetic modeling:

We previously extracted TSCs from CSF and tissue compartments from DCE-MRI studies focused on characterizing the effect of different body postures on glymphatic system transport in rodents (Lee, et al., 2015). We used a Logan plot to calculate the tissue distribution volume V(t) of the Gd-DTPA tracer over the predefined time (~3hrs) and implemented a 2-tissue compartment model to derive information on tracer tissue 'retention' and 'loss' (Lee, et al., 2015). The 2-compartment model allowed us to incorporate the slower and heterogeneous movement of Gd-contrast more accurately in the brain tissue compartment in comparison to CSF and peri-arterial conduits. More recently, we used the CSF and tissue TSCs to model and quantify glymphatic transport kinetics using a 1-tissue compartment model and TSC representing Gd-concentrations derived from the T1 mapping approach (Mortensen, et al., 2019). Fig. 4 shows the processing steps involved in the 1-tissue compartment analysis from CSF and brain tissue compartments. The first step involves segmenting the corresponding anatomical template for the DCE-MRI glymphatic study into a CSF and parenchymal compartment using voxel based morphometric analysis (Koundal et al., 2019, Lee, et al., 2020). The TSC from the CSF and tissue compartments are used as input into the 1-compartment model to derive the influx and efflux rate constants as well as the total tissue distribution volume (Fig. 4).

Regularized Optimal Mass Transport (rOMT):

The 1-tissue compartment kinetic model fits whole brain data derived from DCE-MRI and CSF Gd-contrast delivery well and rate constants for quantifying influx and efflux. However, the kinetic tissue models but often fails at the local tissue level due to glymphatic transport heterogeneity as well as in disease states when glymphatic solute transport is compromised. To obtain information on dynamic glymphatic transport at the voxel-level in the live brain we have instead employed methods from optimal mass transport (OMT) (Ratner et al., 2017, Villani, 2009) including a regularized version to study the glymphatic systems (Elkin et al., 2018). The ***regularized OMT*** (rOMT) problem is concerned with the minimization of the kinetic energy functional wherein the advection/diffusion equation is the only *a priori* assumption required; (for more detail see (Koundal, et al., 2020)). The rOMT analysis returns the interpolated density images and velocity fields. We further implemented the Lagrangian formulation for visualizing glymphatic transport flows over

a specific time interval (Koundal, et al., 2020). From the Lagrangian pathlines several biophysical measures can be derived including the total flow volume (size of the pathline network), and the glymphatic transport speed across tissue compartments. Fig. 5 shows examples of rOMT glymphatic analysis of DCE-MRI Gd-DOTA data from a rat anesthetized with dexmedetomidine supplemented with low dose isoflurane. The dynamic information of solute transport within the brain and efflux pathways derived from rOMT analysis is unique. For example, the color-coded local speed map shows that solute speed trajectories are fast in the CSF compartment and slow down in parenchyma (Fig. 5B). The velocity flux vector analysis captures the direction and strength (vector magnitude) of solute movement over the pre-defined time window. Along the circle of Willis on the ventral surface of the brain, solute transport from the perivascular space into parenchyma can be appreciated (Figs. 5C, D). For more details about rOMT data interpretation see Koundal et al., (Koundal, et al., 2020).

Glymphatic system evaluated by 2-deoxy-2-[^{18}F]fluoroglucose PET-CT

Here we also want to introduce a novel approach to capture glymphatic transport and drainage using PET-CT in combination with administration of 2-deoxy-2-[^{18}F]fluoroglucose (18FDG) into CSF. Positron emission tomography (PET) technology allows to measure with high sensitivity the concentration of positron labelled radiotracers as a function of time in living tissues (Alluri et al., 2020, Fowler et al., 2003, Fowler et al., 2004, Volkow et al., 2003). In the brain the use of PET in combination with a diverse set of radiotracers has been used to measure the regional brain concentration of receptors, enzymes and transporters as well as the transport and pharmacokinetics of molecules such as acetate or of drugs such as cocaine (Ashok et al., 2017, Fowler et al., 1999, Volkow et al., 2013, Volkow et al., 2017). PET has also been used to measure physiological processes such as glucose metabolism, which is done using 18FDG a surrogate of glucose that is trapped intracellularly when it is phosphorylated by hexokinase as part of the metabolic cycle (Fowler and Ido, 2002, Fowler, et al., 2004). Typically, PET studies are performed by injecting the radiotracer intravenously and measuring its concentration in the brain (or other tissues). In our PET studies to study the glymphatic system in the rat we injected 18FDG into the CSF via the cisterna magna in order to measure the pharmacokinetics of FDG from CSF into the brain tissue. To compare the CSF data with the conventional intravenous (i.v.) administration we also included rats who received 18FDG intravenously. For the glymphatic experiments, we anesthetized 4 female rats with barbiturate (see **supplemental methods**) and acquired a CT scan covering the head and thorax followed by a dynamic PET scans obtained at 5-min intervals for a total of ~1.5 hours. For the i.v. experiments we anesthetized 4 female rats with barbiturates and after the CT scan the 18FDG dynamic PET scans were obtained at 5-min intervals for a total of 1 hr using the same field-of-view as for the CSF experiments. Fig. 6 shows 3D volume rendered color-coded 18FDG brain images overlaid on the corresponding anatomical CT images obtained at different times after 18FDG administration. Figs. 6A–C show the 18FDG uptake from CSF and at the initial scan times 18FDG is distributed mainly in the basal cistern (cisterna magna) and spinal column space and after 60 minutes 18FDG can be observed along the ventral surface of the CSF, in the brain tissue, nasal conchae as well as in the heart. At 90 min there is increased uptake in brain and nasal conchae. The corresponding

time activity curves (TAC) are shown in Fig. 6G and demonstrate that 18FDG activity peaks at ~25min from the time of CSF administration and then decays over time. TACs from the nasal conchae (representing glymphatic 'efflux') show a slow and steady increase after 20min of CSF circulation (Fig. 6G). For comparison, we also show corresponding the dynamic 18FDG images after intravenous administration obtain in the other series of rats (Figs. 6D–F). The 18FDG TAC from brain and nasal conchae after i.v. administration of the radiotracer shows rapid increase and reaches a plateau after ~35min where the 18FDG is trapped intracellularly as has been shown previously (Shimoji et al., 2004).

Although this is a preliminary study, the time course of 18FDG uptake is clearly different for the CSF vs. i.v. administration and suggests rich possibilities for analysis, from more complex kinetic models to simple ratio measures that might reflect clearance rates. For example, at late times (>70 min after CSF administration) the brain and nasal conchae levels change relatively linearly with time (brain decreasing and conchae increasing), suggesting that the ratio of conchae to brain is also a stable linear function of time whose slope may be quite sensitive to clearance rate from the brain. Although the spatial resolution of PET is generally inferior to MRI, these studies suggest that it is sufficient for the study of the glymphatic system in the rat brain on at least global and regional scales. An important advantage is that fully quantified PET images directly reflect mass concentrations of the tracer with minimal assumptions with no inherent dependence on disease state of the tissue. Moreover, to avoid potentially confounding effects of anesthesia, PET studies can be carried out in the conscious state using multiple approaches (Kyme et al., 2018, Miranda et al., 2019, Schulz et al., 2011). As such, PET could develop into a standalone approach to the study of glymphatic function, and/or be used to validate the MRI approaches using dual-labeled probes and the new generation of simultaneous PET/MRI scanners. In addition, alternate PET radio-lαβeled tracers should be considered apart from 18FDG which is a metabolically active molecule which is trapped by brain cells and therefore would not easily provide information on efflux or 'clearance' from glymphatic to the lymphatic drainage routs. Another metabolically active tracer would be ^{15}O-water which when injected into the cisterna magna could track water movement from CSF spaces into brain parenchyma and theoretically would have the ability to quantify the movement of water - driven by osmotic active substances - in neuropil and via the glymphatic system. However, a limitation is the very short half-life (2 min) of ^{15}O-water which would limit its application for studying glymphatic-lymphatic transport in the live CNS. Potential alternate tracer candidates for PET based studies of glymphatic and lymphatic transport would ideally be metabolically inert molecules. In DCE-MRI studies Gd-tagged small MW metabolically inert molecules are typically used which are transported in CSF and interstitial fluid of the CNS and which do not normally cross the blood brain barrier. Such radioligands would include 18F-labeled albumin which has gained some interest for lymphatic imaging (Wang et al., 2015) and which should track glymphatic transport in a pattern similar to that observed in DCE-MRI studies and theoretically also efflux to the lymphatic system. Finally, for studying amyloid beta (Aβ) clearance radiotracers that bind to soluble Aβ would be needed which currently are not available. Clearly more studies are needed to explore the full potential of PET for the study of glymphatic system function.

Supplementary Material

Refer to Web version on PubMed Central for supplementary material.

References:

Abbott NJ, Pizzo ME, Preston JE, Janigro D, Thorne RG (2018), The role of brain barriers in fluid movement in the CNS: is there a 'glymphatic' system? Acta Neuropathol 135:387–407. [PubMed: 29428972]

Agency FD, Dotarem - FDA.

Alluri SR, Kim SW, Volkow ND, Kil KE (2020), PET Radiotracers for CNS-Adrenergic Receptors: Developments and Perspectives. Molecules 25.

Antila S, Karaman S, Nurmi H, Airavaara M, Voutilainen MH, Mathivet T, Chilov D, Li Z, et al. (2017), Development and plasticity of meningeal lymphatic vessels. J Exp Med 214:3645–3667. [PubMed: 29141865]

Ashok AH, Mizuno Y, Volkow ND, Howes OD (2017), Association of Stimulant Use With Dopaminergic Alterations in Users of Cocaine, Amphetamine, or Methamphetamine: A Systematic Review and Meta-analysis. JAMA Psychiatry 74:511–519. [PubMed: 28297025]

Aspelund A, Antila S, Proulx ST, Karlsen TV, Karaman S, Detmar M, Wiig H, Alitalo K (2015), A dural lymphatic vascular system that drains brain interstitial fluid and macromolecules. J Exp Med 212:991–999. [PubMed: 26077718]

Barbier EL, Liu L, Grillon E, Payen JF, Lebas JF, Segebarth C, Remy C (2005), Focal brain ischemia in rat: acute changes in brain tissue T1 reflect acute increase in brain tissue water content. NMR Biomed 18:499–506. [PubMed: 16206135]

Benveniste H, Lee H, Ding F, Sun Q, Al-Bizri E, Makaryus R, Probst S, Nedergaard M, et al. (2017), Anesthesia with Dexmedetomidine and Low-dose Isoflurane Increases Solute Transport via the Glymphatic Pathway in Rat Brain When Compared with High-dose Isoflurane. Anesthesiology 127:976–988. [PubMed: 28938276]

Benveniste H, Liu X, Koundal S, Sanggaard S, Lee H, Wardlaw J (2019), The Glymphatic System and Waste Clearance with Brain Aging: A Review. Gerontology 65:106–119. [PubMed: 29996134]

Brinker T, Stopa E, Morrison J, Klinge P (2014), A new look at cerebrospinal fluid circulation. Fluids Barriers CNS 11:10. [PubMed: 24817998]

Cai X, Qiao J, Kulkarni P, Harding IC, Ebong E, Ferris CF (2020), Imaging the effect of the circadian light-dark cycle on the glymphatic system in awake rats. Proc Natl Acad Sci U S A 117:668–676. [PubMed: 31848247]

Da Mesquita S, Fu Z, Kipnis J (2018), The Meningeal Lymphatic System: A New Player in Neurophysiology. Neuron 100:375–388. [PubMed: 30359603]

Davoodi-Bojd E, Ding G, Zhang L, Li Q, Li L, Chopp M, Zhang Z, Jiang Q (2019), Modeling glymphatic system of the brain using MRI. Neuroimage 188:616–627. [PubMed: 30578928]

De Koninck J, Lorrain D, Gagnon P (1992), Sleep positions and position shifts in five age groups: an ontogenetic picture. Sleep 15:143–149. [PubMed: 1579788]

Deike-Hofmann K, Reuter J, Haase R, Paech D, Gnirs R, Bickelhaupt S, Forsting M, Heussel CP, et al. (2019), Glymphatic Pathway of Gadolinium-Based Contrast Agents Through the Brain: Overlooked and Misinterpreted. Invest Radiol 54:229–237. [PubMed: 30480554]

Di Palma C, Goulay R, Chagnot S, Martinez De Lizarrondo S, Anfray A, Salaun JP, Maubert E, Lechapt-Zalcman E, et al. (2018), Cerebrospinal fluid flow increases from newborn to adult stages. Dev Neurobiol 78:851–858. [PubMed: 30027587]

Ding G, Chopp M, Li L, Zhang L, Davoodi-Bojd E, Li Q, Zhang Z, Jiang Q (2018), MRI investigation of glymphatic responses to Gd-DTPA infusion rates. J Neurosci Res 96:1876–1886. [PubMed: 30272825]

Dyke JP, Xu HS, Verma A, Voss HU, Chazen JL (2020), MRI characterization of early CNS transport kinetics post intrathecal gadolinium injection: Trends of subarachnoid and parenchymal distribution in healthy volunteers. Clin Imaging 68:1–6. [PubMed: 32544736]

Edeklev CS, Halvorsen M, Lovland G, Vatnehol SAS, Gjertsen O, Nedregaard B, Sletteberg R, Ringstad G, et al. (2019), Intrathecal Use of Gadobutrol for Glymphatic MR Imaging: Prospective Safety Study of 100 Patients. AJNR Am J Neuroradiol 40:1257–1264. [PubMed: 31320462]

Eide PK, Ringstad G (2015), MRI with intrathecal MRI gadolinium contrast medium administration: a possible method to assess glymphatic function in human brain. Acta Radiol Open 4:2058460115609635. [PubMed: 26634147]

Eide PK, Ringstad G (2018), Delayed clearance of cerebrospinal fluid tracer from entorhinal cortex in idiopathic normal pressure hydrocephalus: A glymphatic magnetic resonance imaging study. J Cereb Blood Flow Metab:271678X18760974.

Eide PK, Vatnehol SAS, Emblem KE, Ringstad G (2018), Magnetic resonance imaging provides evidence of glymphatic drainage from human brain to cervical lymph nodes. Sci Rep 8:7194. [PubMed: 29740121]

Elkin R, Nadeem S, Haber E, Steklova K, Lee H, Benveniste H, Tannenbaum A (2018), GlymphVIS: Visualizing Glymphatic Transport Pathways Using Regularized Optimal Transport. Med Image Comput Comput Assist Interv 11070:844–852. [PubMed: 30906935]

Fournier AP, Gauberti M, Quenault A, Vivien D, Macrez R, Docagne F (2019), Reduced spinal cord parenchymal cerebrospinal fluid circulation in experimental autoimmune encephalomyelitis. J Cereb Blood Flow Metab 39:1258–1265. [PubMed: 29376456]

Fowler JS, Ding YS, Volkow ND (2003), Radiotracers for positron emission tomography imaging. Semin Nucl Med 33:14–27. [PubMed: 12605354]

Fowler JS, Ido T (2002), Initial and subsequent approach for the synthesis of 18FDG. Semin Nucl Med 32:6–12. [PubMed: 11839070]

Fowler JS, Volkow ND, Ding YS, Wang GJ, Dewey S, Fischman MW, Foltin R, Hitzemann R (1999), Positron emission tomography studies of dopamine-enhancing drugs. J Clin Pharmacol 39:13S–16S. [PubMed: 10434242]

Fowler JS, Volkow ND, Wang GJ, Ding YS (2004), 2-deoxy-2-[18F]fluoro-D-glucose and alternative radiotracers for positron emission tomography imaging using the human brain as a model. Semin Nucl Med 34:112–121. [PubMed: 15031811]

Gaberel T, Gakuba C, Goulay R, Martinez De Lizarrondo S, Hanouz JL, Emery E, Touze E, Vivien D, et al. (2014), Impaired glymphatic perfusion after strokes revealed by contrast-enhanced MRI: a new target for fibrinolysis? Stroke 45:3092–3096. [PubMed: 25190438]

Gakuba C, Gaberel T, Goursaud S, Bourges J, Di Palma C, Quenault A, Martinez de Lizarrondo S, Vivien D, et al. (2018), General Anesthesia Inhibits the Activity of the "Glymphatic System". Theranostics 8:710–722. [PubMed: 29344300]

Goulay R, Aron Badin R, Flament J, Emery E, Hantraye P, Vivien D, Gaberel T (2018), Cerebrospinal fluid leakage after posterior fossa surgery may impair brain metabolite clearance. Neurochirurgie 64:422–424. [PubMed: 30477647]

Goulay R, Flament J, Gauberti M, Naveau M, Pasquet N, Gakuba C, Emery E, Hantraye P, et al. (2017), Subarachnoid Hemorrhage Severely Impairs Brain Parenchymal Cerebrospinal Fluid Circulation in Nonhuman Primate. Stroke 48:2301–2305. [PubMed: 28526764]

Hadjihambi A, Harrison IF, Costas-Rodriguez M, Vanhaecke F, Arias N, Gallego-Duran R, Mastitskaya S, Hosford PS, et al. (2019), Impaired brain glymphatic flow in experimental hepatic encephalopathy. J Hepatol 70:40–49. [PubMed: 30201461]

Halliburton WD (1917), Presidential Address: The Possible Functions of the Cerebrospinal Fluid. Proc R Soc Med 10:1–12.

Harrison IF, Ismail O, Machhada A, Colgan N, Ohene Y, Nahavandi P, Ahmed Z, Fisher A, et al. (2020), Impaired glymphatic function and clearance of tau in an Alzheimer's disease model. Brain 143:2576–2593. [PubMed: 32705145]

Haughton VM, Korosec FR, Medow JE, Dolar MT, Iskandar BJ (2003), Peak systolic and diastolic CSF velocity in the foramen magnum in adult patients with Chiari I malformations and in normal control participants. AJNR Am J Neuroradiol 24:169–176. [PubMed: 12591629]

Hladky SB, Barrand MA (2014), Mechanisms of fluid movement into, through and out of the brain: evaluation of the evidence. Fluids Barriers CNS 11:26. [PubMed: 25678956]

Huber VJ, Igarashi H, Ueki S, Kwee IL, Nakada T (2018), Aquaporin-4 facilitator TGN-073 promotes interstitial fluid circulation within the blood-brain barrier: [17O]H2O JJVCPE MRI study. Neuroreport 29:697–703. [PubMed: 29481527]

Iliff JJ, Chen MJ, Plog BA, Zeppenfeld DM, Soltero M, Yang L, Singh I, Deane R, et al. (2014), Impairment of glymphatic pathway function promotes tau pathology after traumatic brain injury. J Neurosci 34:16180–16193. [PubMed: 25471560]

Iliff JJ, Lee H, Yu M, Feng T, Logan J, Nedergaard M, Benveniste H (2013), Brain-wide pathway for waste clearance captured by contrast-enhanced MRI. J Clin Invest 123:1299–1309. [PubMed: 23434588]

Iliff JJ, Wang M, Liao Y, Plogg BA, Peng W, Gundersen GA, Benveniste H, Vates GE, et al. (2012), A paravascular pathway facilitates CSF flow through the brain parenchyma and the clearance of interstitial solutes, including amyloid beta. Sci Transl Med 4:147ra111.

Jacob L, Boisserand LSB, Geraldo LHM, de Brito Neto J, Mathivet T, Antila S, Barka B, Xu Y, et al. (2019), Anatomy and function of the vertebral column lymphatic network in mice. Nat Commun 10:4594. [PubMed: 31597914]

Jacobsen HH, Ringstad G, Jorstad OK, Moe MC, Sandell T, Eide PK (2019), The Human Visual Pathway Communicates Directly With the Subarachnoid Space. Invest Ophthalmol Vis Sci 60:2773–2780. [PubMed: 31247084]

Jiang Q, Zhang L, Ding G, Davoodi-Bojd E, Li Q, Li L, Sadry N, Nedergaard M, et al. (2016), Impairment of the glymphatic system after diabetes. J Cereb Blood Flow Metab.

Jiang Q, Zhang L, Ding G, Davoodi-Bojd E, Li Q, Li L, Sadry N, Nedergaard M, et al. (2017), Impairment of the glymphatic system after diabetes. J Cereb Blood Flow Metab 37:1326–1337. [PubMed: 27306755]

Johnston M (2003), The importance of lymphatics in cerebrospinal fluid transport. Lymphat Res Biol 1:41–44; discussion 45. [PubMed: 15624320]

Karimy JK, Kahle KT, Kurland DB, Yu E, Gerzanich V, Simard JM (2015), A novel method to study cerebrospinal fluid dynamics in rats. J Neurosci Methods 241:78–84. [PubMed: 25554415]

Kato Y, Bokura K, Taoka T, Naganawa S (2019), Increased signal intensity of low-concentration gadolinium contrast agent by longer repetition time in heavily T2-weighted-3D-FLAIR. Jpn J Radiol 37:431–435. [PubMed: 30863972]

Koundal S, Elkin R, Nadeem S, Xue Y, Constantinou S, Sanggaard S, Liu X, Monte B, et al. (2020), Optimal Mass Transport with Lagrangian Workflow Reveals Advective and Diffusion Driven Solute Transport in the Glymphatic System. Sci Rep 10:1990. [PubMed: 32029859]

Koundal S, Liu X, Sanggaard S, Mortensen K, Wardlaw J, Nedergaard M, Benveniste H, Lee H (2019), Brain Morphometry and Longitudinal Relaxation Time of Spontaneously Hypertensive Rats (SHRs) in Early and Intermediate Stages of Hypertension Investigated by 3D VFA-SPGR MRI. Neuroscience 404:14–26. [PubMed: 30690138]

Kyme AZ, Angelis GI, Eisenhuth J, Fulton RR, Zhou V, Hart G, Popovic K, Akhtar M, et al. (2018), Open-field PET: Simultaneous brain functional imaging and behavioural response measurements in freely moving small animals. Neuroimage 188:92–101. [PubMed: 30502443]

Lee H, Mortensen K, Sanggaard S, Koch P, Brunner H, Quistorff B, Nedergaard M, Benveniste H (2018), Quantitative Gd-DOTA uptake from cerebrospinal fluid into rat brain using 3D VFA-SPGR at 9.4T. Magn Reson Med 79:1568–1578. [PubMed: 28627037]

Lee H, Xie L, Yu M, Kang H, Feng T, Deane R, Logan J, Nedergaard M, et al. (2015), The Effect of Body Posture on Brain Glymphatic Transport. J Neurosci 35:11034–11044. [PubMed: 26245965]

Lee H, Xu F, Liu X, Koundal S, Zhu X, Davis J, Yanez D, Schrader J, et al. (2020), Diffuse white matter loss in a transgenic rat model of cerebral amyloid angiopathy. J Cereb Blood Flow Metab:271678X20944226.

Li L, Chopp M, Ding G, Davoodi-Bojd E, Zhang L, Li Q, Zhang Y, Xiong Y, et al. (2020), MRI detection of impairment of glymphatic function in rat after mild traumatic brain injury. Brain Res 1747:147062. [PubMed: 32818526]

Lin L, Hao X, Li C, Sun C, Wang X, Yin L, Zhang X, Tian J, et al. (2020), Impaired glymphatic system in secondary degeneration areas after ischemic stroke in rats. J Stroke Cerebrovasc Dis 29:104828. [PubMed: 32404284]

Louveau A, Harris TH, Kipnis J (2015), Revisiting the Mechanisms of CNS Immune Privilege. Trends Immunol 36:569–577. [PubMed: 26431936]

Louveau A, Herz J, Alme MN, Salvador AF, Dong MQ, Viar KE, Herod SG, Knopp J, et al. (2018), CNS lymphatic drainage and neuroinflammation are regulated by meningeal lymphatic vasculature. Nat Neurosci 21:1380–1391. [PubMed: 30224810]

Louveau A, Plog BA, Antila S, Alitalo K, Nedergaard M, Kipnis J (2017), Understanding the functions and relationships of the glymphatic system and meningeal lymphatics. J Clin Invest 127:3210–3219. [PubMed: 28862640]

Louveau A, Smirnov I, Keyes TJ, Eccles JD, Rouhani SJ, Peske JD, Derecki NC, Castle D, et al. (2015), Structural and functional features of central nervous system lymphatic vessels. Nature 523:337–341. [PubMed: 26030524]

Ma Y, Smith D, Hof PR, Foerster B, Hamilton S, Blackband SJ, Yu M, Benveniste H (2008), In Vivo 3D Digital Atlas Database of the Adult C57BL/6J Mouse Brain by Magnetic Resonance Microscopy. Front Neuroanat 2:1. [PubMed: 18958199]

Meng Y, Abrahao A, Heyn CC, Bethune AJ, Huang Y, Pople CB, Aubert I, Hamani C, et al. (2019), Glymphatics Visualization after Focused Ultrasound-Induced Blood-Brain Barrier Opening in Humans. Ann Neurol 86:975–980. [PubMed: 31525269]

Mestre H, Du T, Sweeney AM, Liu G, Samson AJ, Peng W, Mortensen KN, Staeger FF, et al. (2020), Cerebrospinal fluid influx drives acute ischemic tissue swelling. Science 367.

Mestre H, Hablitz LM, Xavier AL, Feng W, Zou W, Pu T, Monai H, Murlidharan G, et al. (2018), Aquaporin-4-dependent glymphatic solute transport in the rodent brain. Elife 7.

Mestre H, Mori Y, Nedergaard M (2020), The Brain's Glymphatic System: Current Controversies. Trends Neurosci 43:458–466. [PubMed: 32423764]

Mestre H, Tithof J, Du T, Song W, Peng W, Sweeney AM, Olveda G, Thomas JH, et al. (2018), Flow of cerebrospinal fluid is driven by arterial pulsations and is reduced in hypertension. Nat Commun 9:4878. [PubMed: 30451853]

Miranda A, Kang MS, Blinder S, Bouhachi R, Soucy JP, Aliaga-Aliaga A, Massarweh G, Stroobants S, et al. (2019), PET imaging of freely moving interacting rats. Neuroimage 191:560–567. [PubMed: 30831313]

Morris AW, Sharp MM, Albargothy NJ, Fernandes R, Hawkes CA, Verma A, Weller RO, Carare RO (2016), Vascular basement membranes as pathways for the passage of fluid into and out of the brain. Acta Neuropathol 131:725–736. [PubMed: 26975356]

Mortensen KN, Sanggaard S, Mestre H, Lee H, Kostrikov S, Xavier ALR, Gjedde A, Benveniste H, et al. (2019), Impaired Glymphatic Transport in Spontaneously Hypertensive Rats. J Neurosci 39:6365–6377. [PubMed: 31209176]

Mott FW (1910), The Oliver-Sharpey Lectures on the cerebrospinal fluid. The Lancet (British edition) ii:1–8.

Naganawa S, Ito R, Taoka T, Yoshida T, Sone M (2020), The Space between the Pial Sheath and the Cortical Venous Wall May Connect to the Meningeal Lymphatics. Magn Reson Med Sci 19:1–4. [PubMed: 31611540]

Naganawa S, Nakane T, Kawai H, Taoka T (2017), Gd-based Contrast Enhancement of the Perivascular Spaces in the Basal Ganglia. Magn Reson Med Sci 16:61–65. [PubMed: 27430361]

Ohno K, Samaranch L, Hadaczek P, Bringas JR, Allen PC, Sudhakar V, Stockinger DE, Snieckus C, et al. (2019), Kinetics and MR-Based Monitoring of AAV9 Vector Delivery into Cerebrospinal Fluid of Nonhuman Primates. Mol Ther Methods Clin Dev 13:47–54. [PubMed: 30666308]

Pardridge WM (2016), CSF, blood-brain barrier, and brain drug delivery. Expert Opin Drug Deliv 13:963–975. [PubMed: 27020469]

Plog BA, Dashnaw ML, Hitomi E, Peng W, Liao Y, Lou N, Deane R, Nedergaard M (2015), Biomarkers of traumatic injury are transported from brain to blood via the glymphatic system. J Neurosci 35:518–526. [PubMed: 25589747]

Raper D, Louveau A, Kipnis J (2016), How Do Meningeal Lymphatic Vessels Drain the CNS? Trends Neurosci 39:581–586. [PubMed: 27460561]

Ratner V, Gao Y, Lee H, Elkin R, Nedergaard M, Benveniste H, Tannenbaum A (2017), Cerebrospinal and interstitial fluid transport via the glymphatic pathway modeled by optimal mass transport. Neuroimage 152:530–537. [PubMed: 28323163]

Ratner V, Zhu L, Kolesov I, Nedergaard M, Benveniste H, Tannenbaum A (2015), Optimal-mass-transfer-based estimation of glymphatic transport in living brain. Proc SPIE Int Soc Opt Eng 9413.

Rennels ML, Gregory TF, Blaumanis OR, Fujimoto K, Grady PA (1985), Evidence for a 'paravascular' fluid circulation in the mammalian central nervous system, provided by the rapid distribution of tracer protein throughout the brain from the subarachnoid space. Brain Res 326:47–63. [PubMed: 3971148]

Ringstad G, Valnes LM, Dale AM, Pripp AH, Vatnehol SS, Emblem KE, Mardal KA, Eide PK (2018), Brain-wide glymphatic enhancement and clearance in humans assessed with MRI. JCI Insight 3.

Ringstad G, Vatnehol SAS, Eide PK (2017), Glymphatic MRI in idiopathic normal pressure hydrocephalus. Brain 140:2691–2705. [PubMed: 28969373]

Schulz D, Southekal S, Junnarkar SS, Pratte J-F, Purschke ML, Stoll SP, Ravindranath B, Maramraju SH, et al. (2011), Simultaneous assessment of rodent behavior and neurochemistry using a miniature positron emission tomograph. Nat Meth 8:347–352.

Shimoji K, Ravasi L, Schmidt K, Soto-Montenegro ML, Esaki T, Seidel J, Jagoda E, Sokoloff L, et al. (2004), Measurement of cerebral glucose metabolic rates in the anesthetized rat by dynamic scanning with 18F-FDG, the ATLAS small animal PET scanner, and arterial blood sampling. J Nucl Med 45:665–672. [PubMed: 15073264]

Takano K, Yamada M (2020), Contrast-enhanced magnetic resonance imaging evidence for the role of astrocytic aquaporin-4 water channels in glymphatic influx and interstitial solute transport. Magn Reson Imaging 71:11–16. [PubMed: 32446035]

Taoka T, Jost G, Frenzel T, Naganawa S, Pietsch H (2018), Impact of the Glymphatic System on the Kinetic and Distribution of Gadodiamide in the Rat Brain: Observations by Dynamic MRI and Effect of Circadian Rhythm on Tissue Gadolinium Concentrations. Invest Radiol 53:529–534. [PubMed: 29652699]

Truman LA, N A.G., Bentley KL, Ruddle NH (2013), Lymphatic vessel function in head and neck inflammation. Lymphat Res Biol 11:187–192. [PubMed: 24044758]

Villani C (2009), Optimal Transport: Old and New. Grundlehr Math Wiss 338:1–973.

Volkow ND, Fowler JS, Wang GJ (2003), Positron emission tomography and single-photon emission computed tomography in substance abuse research. Semin Nucl Med 33:114–128. [PubMed: 12756644]

Volkow ND, Kim SW, Wang GJ, Alexoff D, Logan J, Muench L, Shea C, Telang F, et al. (2013), Acute alcohol intoxication decreases glucose metabolism but increases acetate uptake in the human brain. Neuroimage 64:277–283. [PubMed: 22947541]

Volkow ND, Wiers CE, Shokri-Kojori E, Tomasi D, Wang GJ, Baler R (2017), Neurochemical and metabolic effects of acute and chronic alcohol in the human brain: Studies with positron emission tomography. Neuropharmacology 122:175–188. [PubMed: 28108358]

Wang Y, Lang L, Huang P, Wang Z, Jacobson O, Kiesewetter DO, Ali IU, Teng G, et al. (2015), In vivo albumin labeling and lymphatic imaging. Proc Natl Acad Sci U S A 112:208–213. [PubMed: 25535368]

Wardlaw JM, Benveniste H, Nedergaard M, Zlokovic BV, Mestre H, Lee H, Doubal FN, Brown R, et al. (2020), Perivascular spaces in the brain: anatomy, physiology and pathology. Nat Rev Neurol 16:137–153. [PubMed: 32094487]

Watts R, Steinklein JM, Waldman L, Zhou X, Filippi CG (2019), Measuring Glymphatic Flow in Man Using Quantitative Contrast-Enhanced MRI. AJNR Am J Neuroradiol 40:648–651. [PubMed: 30679221]

Weed LH (1922), The cerebrospinal fluid. Physiological Reviews 2:171–203.

Weller RO, Kida S, Zhang ET (1992), Pathways of fluid drainage from the brain--morphological aspects and immunological significance in rat and man. Brain Pathol 2:277–284. [PubMed: 1341963]

Xie L, Kang H, Xu Q, Chen MJ, Liao Y, Thiyagarajan M, O'Donnell J, Christensen DJ, et al. (2013), Sleep drives metabolite clearance from the adult brain. Science 342:373–377. [PubMed: 24136970]

Xue Y, Liu X, Koundal S, Constantinou S, Dai F, Santambrogio L, Lee H, Benveniste H (2020), In vivo T1 mapping for quantifying glymphatic system transport and cervical lymph node drainage. Sci Rep 10:14592. [PubMed: 32884041]

Yang L, Kress BT, Weber HJ, Thiyagarajan M, Wang B, Deane R, Benveniste H, Iliff JJ, et al. (2013), Evaluating glymphatic pathway function utilizing clinically relevant intrathecal infusion of CSF tracer. J Transl Med 11:107. [PubMed: 23635358]

Zhou Y, Cai J, Zhang W, Gong X, Yan S, Zhang K, Luo Z, Sun J, et al. (2020), Impairment of the Glymphatic Pathway and Putative Meningeal Lymphatic Vessels in the Aging Human. Ann Neurol 87:357–369. [PubMed: 31916277]

Highlights:

- Dynamic contrast enhanced MRI and CSF delivery of Gd-based contrast agents is a robust imaging platform for quantifying brain-wide glymphatic transport
- Glymphatic transport and CSF flow dynamics is dependent on body posture
- T1 mapping by MRI can quantify glymphatic transport and drainage to cervical lymph nodes concurrently in the same subject
- Glymphatic transport kinetics are heterogenous across brain regions
- Dynamic solute and fluid transport in the CNS by optimal mass transport analysis requires incorporation of advective as well as diffusion terms
- Glymphatic transport can be measured by positron emission tomography with CSF administration of radioactive ligands

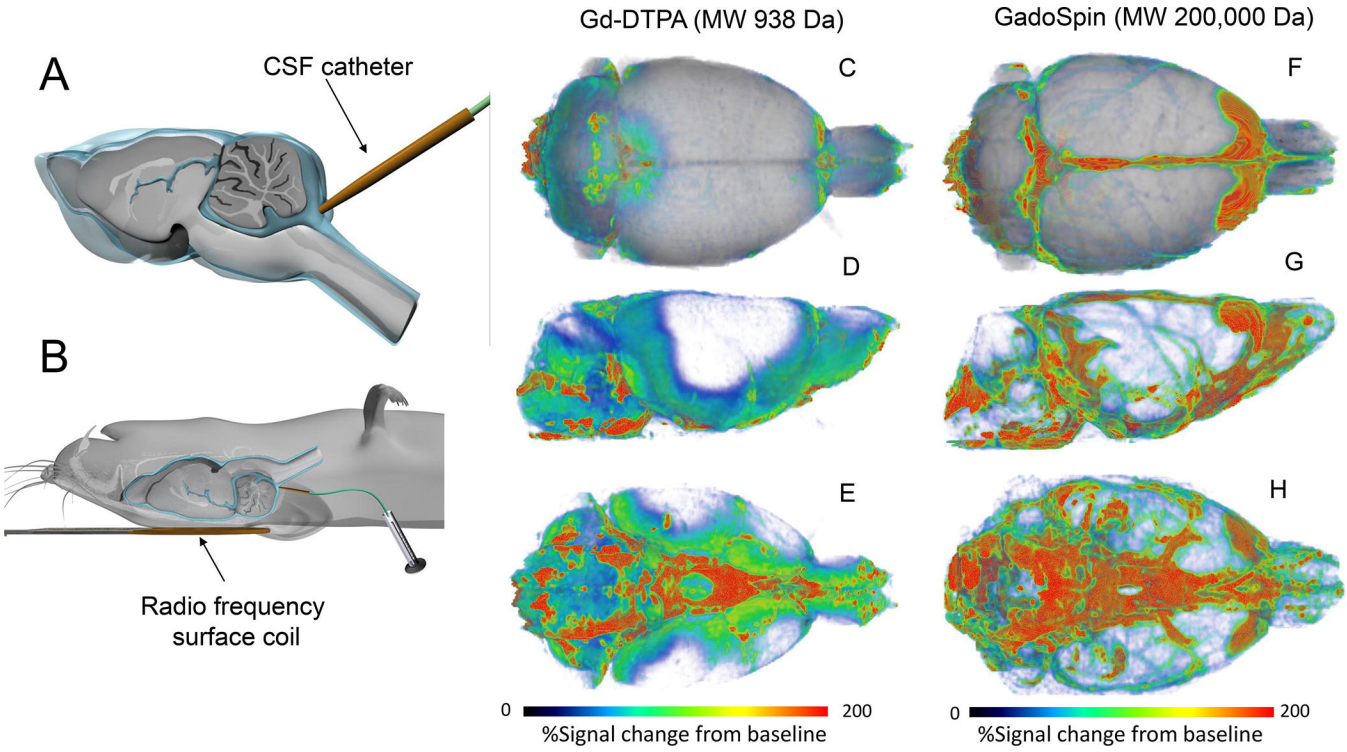

Fig. 1. Overview of dynamic contrast enhanced MRI with Gd-contrast into CSF

A: Illustration of catheter position for Gd- contrast delivery into cerebrospinal fluid (CSF, blue liquid) via the cisterna magna of a rat brain. The rat brain is shown in a sagittal transverse cut to show the CSF compartment (blue) in relation to the brain tissue (grey color). **B**: In preparation for magnetic resonance imaging (MRI) and glymphatic transport, the anesthetized rat with the indwelling CSF catheter is positioned supine with the small radio frequency surface coil placed under the head. **C-E**: 3D volume rendered dynamic contrast enhanced MRI (DCE)-MRI) images of a rat brain in top (**C**), lateral decubitus (**D**) and caudal/ventral view (**E**) are shown ~ 90 min after CSF administration of Gd-DTPA (molecular weight, (MW) 938 Da). The DCE-MRI data has been processed so that the color-coded map represents '% signal change from baseline'. Red and blue colors represent high and low glymphatic transport of Gd-DTPA, respectively. There is high glymphatic uptake of Gd-DTPA into the cerebellum, ventral hippocampus, and olfactory bulb. **F-H**: 3D volume rendered DCE-MRI of another rat ~ 90 min after CSF administration of GadoSpin which is a large molecule (MW 200,000 Da) compared to Gd-DTPA. Again, the color-coded map represents %signal from baseline. The distribution pattern of GadoSpin is remarkably different from Gd-DTPA and the bulk of the signal remains in the CSF compartment and the perivascular space along large arteries on the ventral surface of the brain. There is almost no tissue uptake of GadoSpin over 90 min. DCE-MRI data are from Iliff et al., (Iliff, et al., 2013).

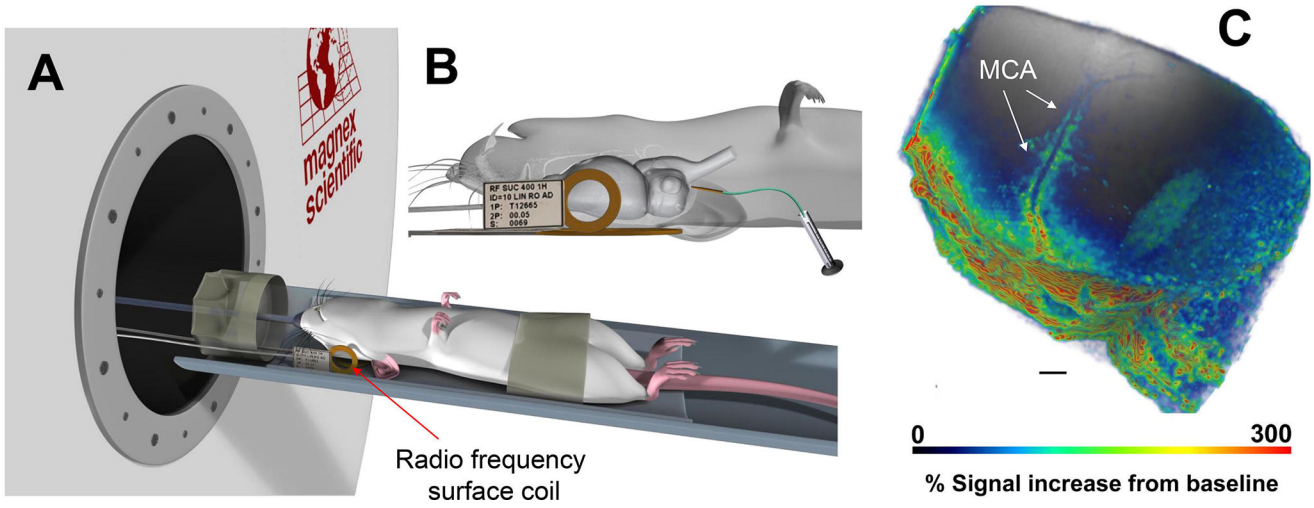

Fig. 2. Dynamic contrast enhanced MRI for tracking perivascular solute transport

A: Illustration of anesthetized rodent positioned supine with the small radio-frequency (RF) surface coil positioned on the lateral side of the head. **B**: Higher magnification of the RF surface coil position with details of the rat brain and indwelling CSF catheter showing that only part of the rat's brain is captured in this experimental set up. **C**: 3D volume rendered MRI of glymphatic transport of 1:5 dilution of Gd-DOTA ~90min after administration into CSF. The higher 'mass' of Gd-DOTA administered enables tracking of solute movement along the middle cerebral artery (MCA). Scale bar = 2mm. Data are from Koundal et al., (Koundal, et al., 2020).

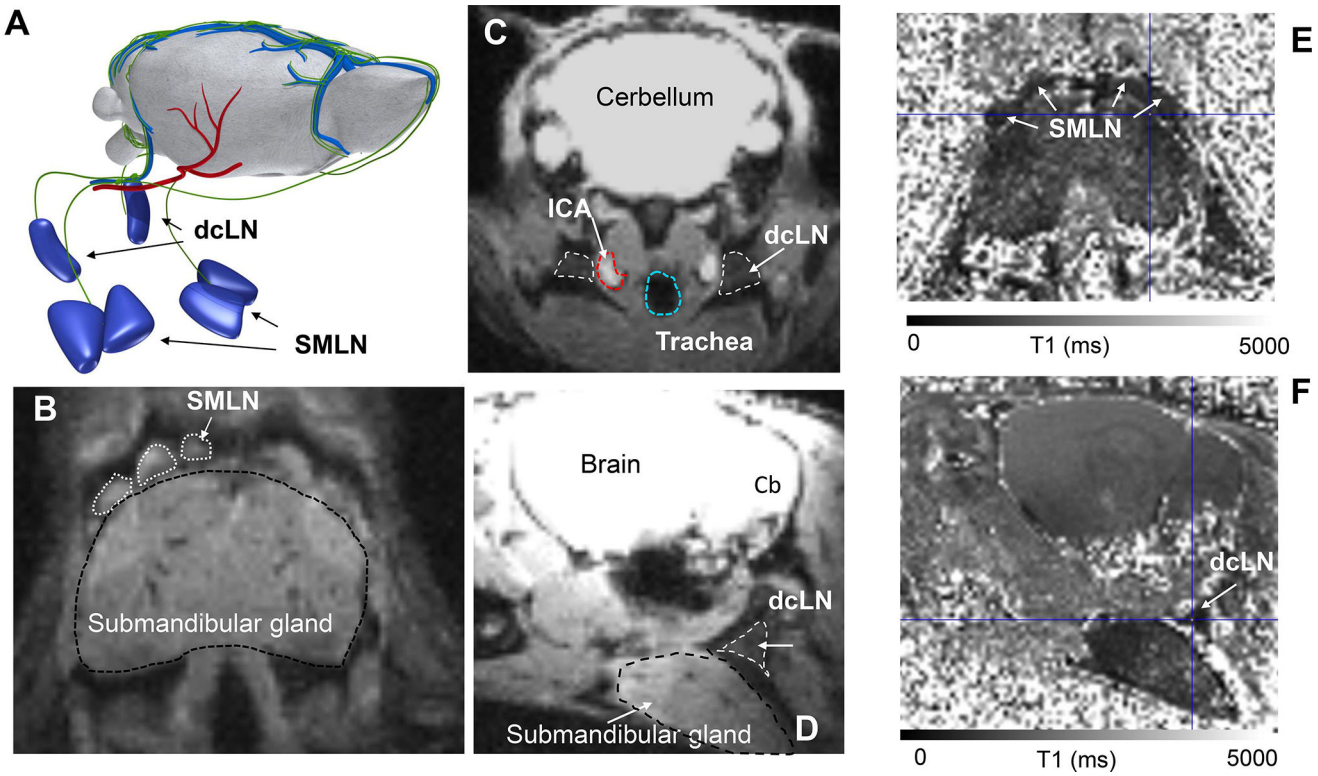

Fig. 3: T1 mapping for quantifying glymphatic and cervical lymph node transport

A: Illustration of the superficial submandibular lymph nodes (SMLN) and deep cervical lymph nodes (dcLN) in relation to the whole rodent brain. The green vasculature represents meningeal and extracranial lymphatic vessels draining to the nodes. We note that the illustration of the afferent draining lymphatics to the nodes are not based on accurate anatomical landmarks. **B:** Proton density weighted (PDW) MRI from a mouse at the level of the submandibular gland showing the position of the SMLN. **C:** PDW MRI from mouse illustrating the position of the dcLN in relation to key anatomical landmarks including the internal carotid artery (ICA) and trachea in an axial cut. **D:** Sagittal cut of the same PDW MRI shown in C, illustrating that the dcLN is positioned deep to the submandibular gland. **E:** Corresponding T1 map from a mouse shown in B after CSF administration of Gd-DOTA. The darkness of the SMLNs indicates that Gd-DOTA has drained from the CSF/brain to the nodes thereby shortening the T1. **F:** The same T1 map as shown in E now sliced at the level of the dcLN which appear as a dark triangle due to uptake of Gd-DOTA. MRI data are from Xue et al., (Xue, et al., 2020).

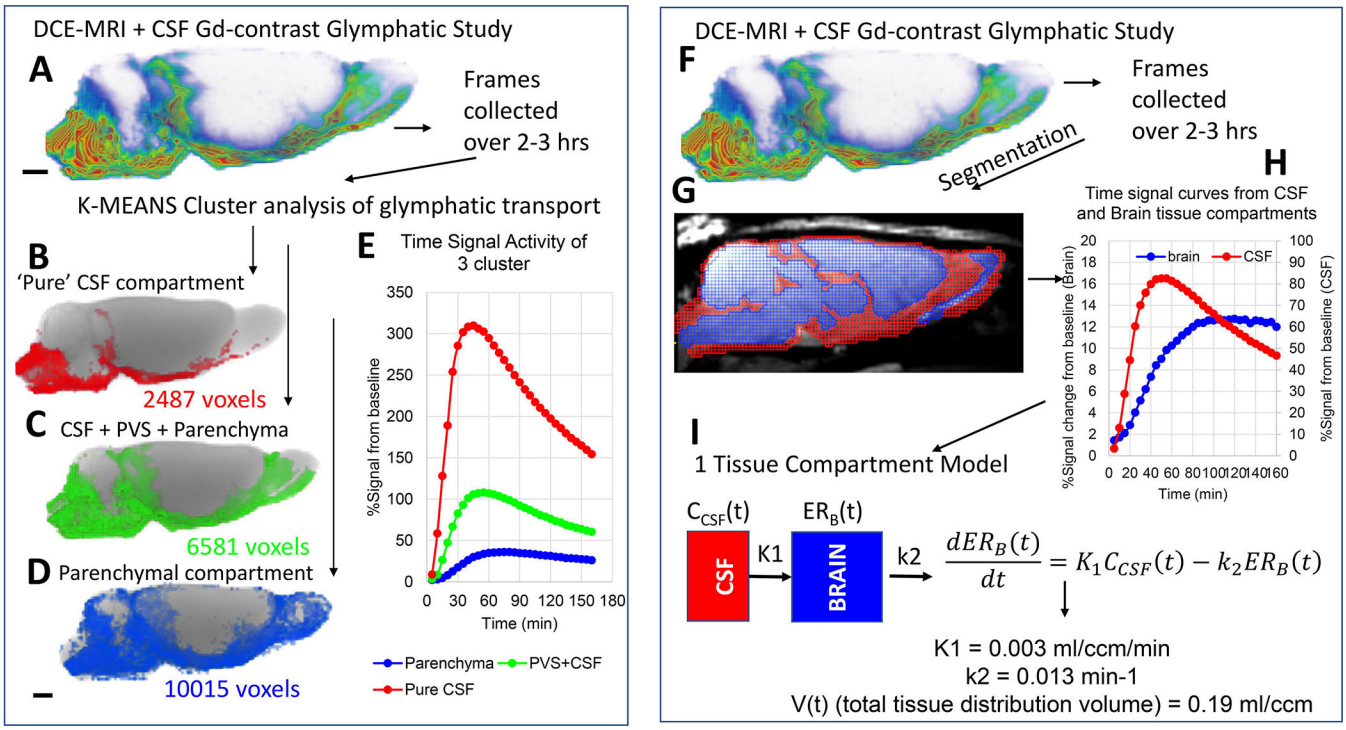

Fig. 4: Glymphatic transport analysis by k-means cluster analysis and kinetic modeling

A: DCE-MRI glymphatic study with CSF Gd-DOTA from a normal 3M old Sprague Dawley rat. The time-series of DCE-MRI images is used as data input for the k-means cluster analysis. **B-D**: Three tissue 'cluster' compartments derived from the cluster analysis are shown as binary volume rendered color-coded masks overlaid on the corresponding anatomical brain. The red cluster (**B**) represents the smallest volume and is located in the CSF compartment proper. The large blue cluster represents 'parenchymal' glymphatic transport (**D**). The green cluster (**C**) represents mixed cluster of subarachnoid CSF, peri-vascular CSF of large arteries as well as adjacent tissue. **E**: The corresponding time signal curves (TSC) from each of the three clusters are shown. The red CSF cluster TSC is characterized by high peak magnitude (~300% signal increase) and rapid decay. The blue parenchymal TSC is characterized by lowest peak signal magnitude and slowest decay when compared to the other two clusters which contain CSF. **F**: DCE-MRI glymphatic study of normal rat. **G**: The red and blue masks overlaid on the MRI represent the CSF and tissue compartment derived using voxel-based morphometry analysis. **H**: The CSF and tissue masks are used to extract TSC from the two compartments. **I**: Mathematical expression of 1-tissue compartment model and the derived quantitative output. K1 = influx rate constant and k2 is the efflux rate constant. For more detail see (Mortensen, et al., 2019).

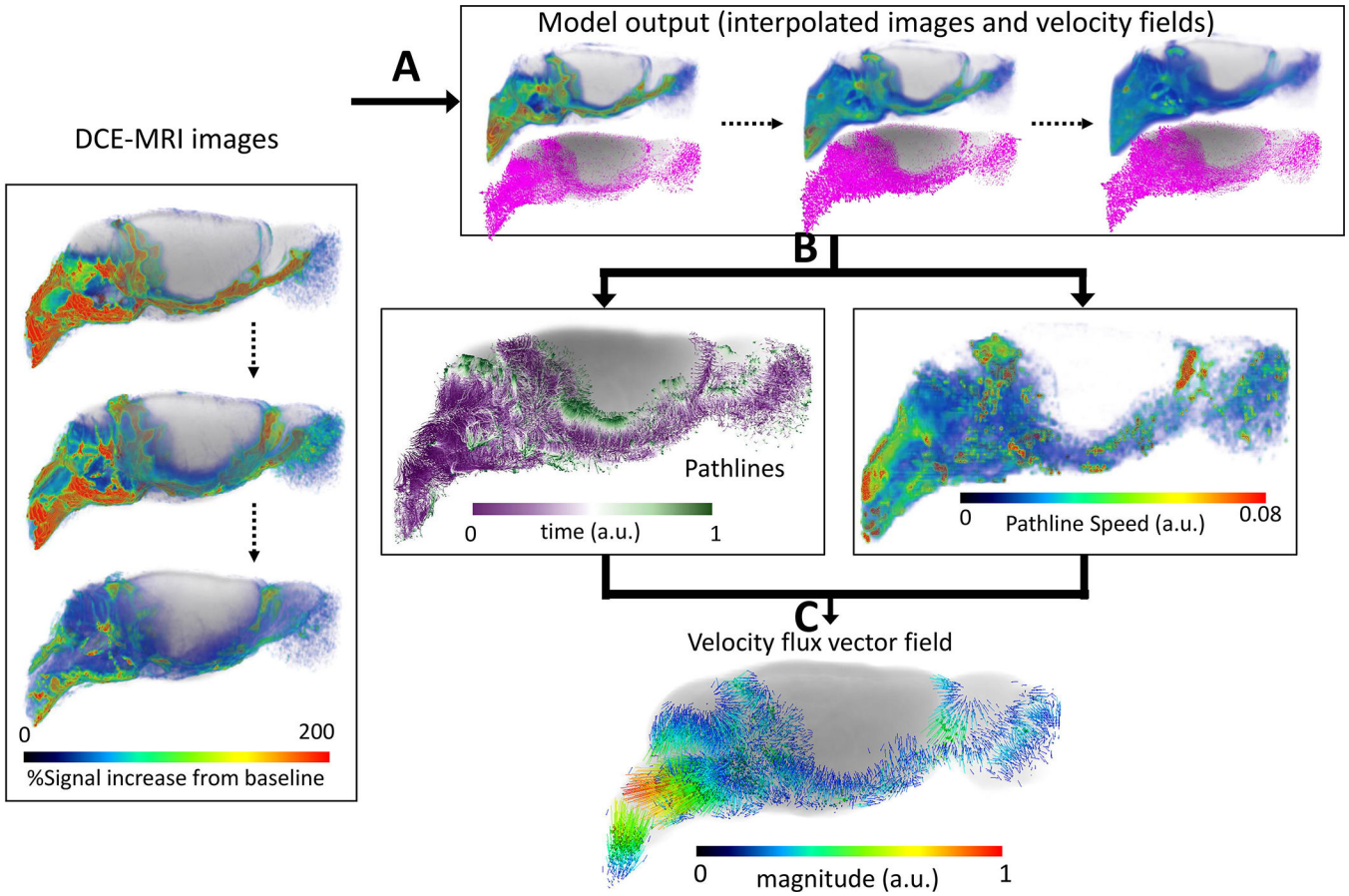

Fig. 5: Regularized optimal mass transport (rOMT) analysis of glymphatic solute transport

Computational processing pipeline of rOMT analysis: **A**: DCE-MRI images over a pre-defined time period (45–210 min) after CSF administration of Gd-DTPA are fed into the transport (rOMT) model which, returns interpolated images and dynamic velocity fields. **B**: Lagrangian dynamic formulation is employed to process the output to obtain glymphatic solute pathlines and pathline speed. The binary pathlines show the trajectories of solute transport and the purple to green color of each pathline represents start points to end points, respectively. The total volume of the pathline network measures the volume of dynamic glymphatic flow. The pathline speed reflects the relative speed within the pathlines which, is used to evaluate transport difference across the brain compartments. **C:** The velocity flux vector field of the pathlines can also be derived and demonstrates the direction and magnitude of glymphatic solute movement. (MRI data are from Benveniste et al., (Benveniste, et al., 2017)).

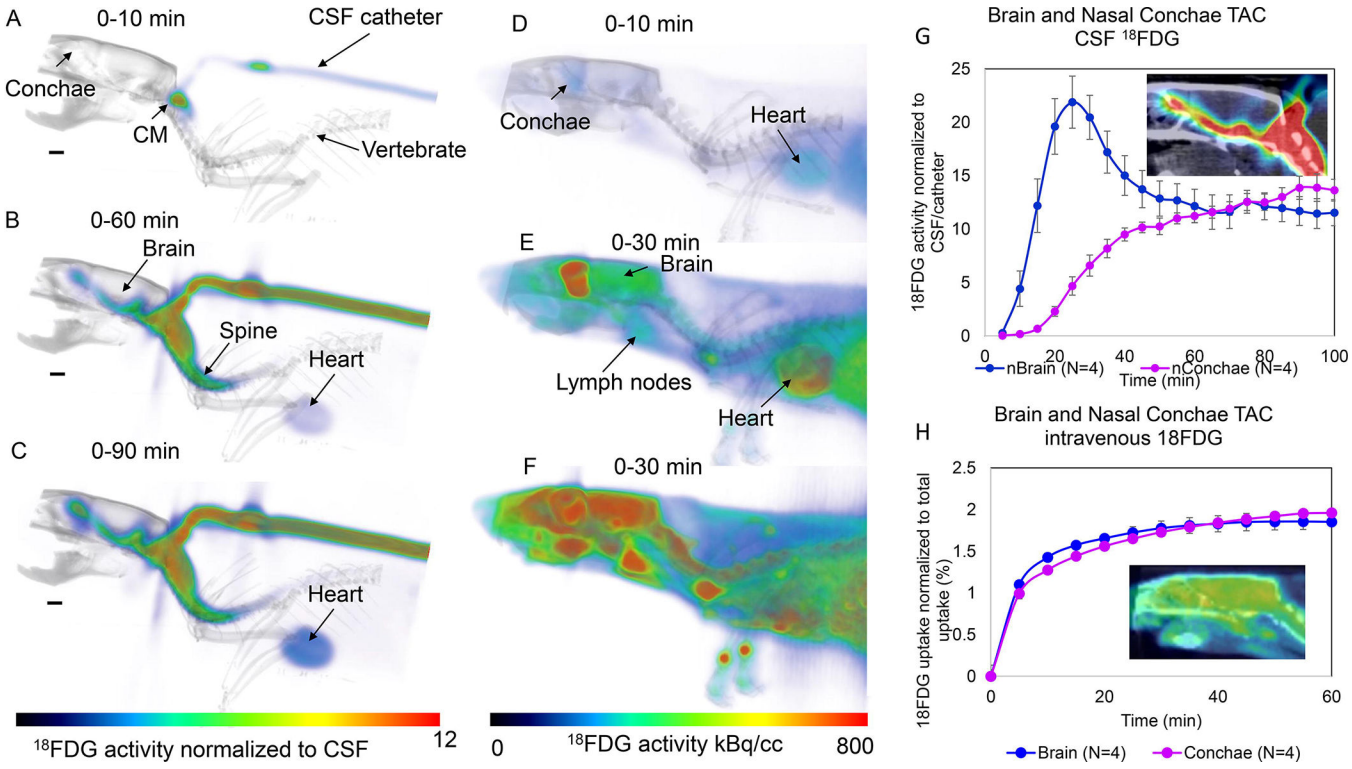

Fig. 6: Brain-wide glymphatic transport in rat brain of 18FDG evaluated by PET-CT

A-C: Dynamic summed 18FDG PET images are shown (A = 0–10min), B = 0–60 min, C = 0–90min from the time of administration of 18FDG into the CSF via the cisterna magna (CM). The 3D volume rendered color-coded maps represent the summed 18FDG activity normalized to activity in the CSF (cisterna magna/catheter) which are overlaid on the corresponding 3D volume rendered image for anatomical landmarking. At the earliest time, 18FDG is presented in the CM only (A), and at later timepoints 18FDG is observed along the ventral surface of the brain/CSF, inside the brain proper as well as in the nasal conchae (**B, C**). Faint uptake in the heart can also be appreciated. **D-F**: Dynamic summed 18FDG PET images are shown from a rat receiving i.v. 18FDG. The 3D volume rendered color coded maps represent 18FDG activity summed over a given time interval to show the uptake pattern over time. At early time after i.v. administration 18FDG uptake is evident in the brain, heart, spine and lymph nodes. **G**: Time activity curves (TAC) from the whole brain and nasal conchae from four rats receiving 18FDG. The data are presented as mean ± SEM. The TAC from brain peaks at ~25 min after the 18FDG administration into the CSF, whereas the TAC from the nasal conchae steadily increase from 40–100min. The insert shows 18FDG activity at 90min overlaid on the CT image. **H**: Corresponding TACs from brain and nasal conchae from 4 rats receiving i.v. 18FDG. There is an immediate increase in activity over the first 10min and plateau is reached at ~35–40min after i.v. 18FDG. The insert shows 18FDG activity at 60min in the brain and nasal conchae overlaid on the corresponding CT image.

Table 1:

A list of DCE-MRI glymphatics studies published 2013-present

Species	Anesthesia	Contrast agent/ molecular weight (MW)	Contrast concentration (mM)	Volume and infusion rate	Magnetic field & sequence	Spatial resolution (mm^3)	Year [Reference]
Rat	Nembutal	Gd-DTPA, MW 938 Da and GadoSpin P (MW 200 kDa;	21 mM Gd-DTPA; 0.17 mM GadoSpin	80 μl 1.6μl/min	9.4T 3D T1-weighted FLASH	0.117 × 0.234 × 0.250 = 0.007 mm^3	2013 (Iliff, et al., 2013)
Mouse	Isoflurane/N_2O	Gadoterate meglumine (DOTAREM)	500mM DOTA-Gd (DOTAREM®,	1μ 1μ/min	7.0T 3D T1-weighted FLASH	0.078 × 0.078 × 0.150 = 0.001 mm^3	2014 (Gaberel, et al., 2014)
Rat	Ketamine/ Xylazine	Gd-DTPA, MW 938 Da	12.5 mM Gd-DTPA	20 μl 1 μl/min	9.4T 3D T1-weighted FLASH; T1 mapping	0.12 × 0.12 × 0.13 mm = 0.002 mm^3	2015 (Lee, et al., 2015)
Human	N/A	Gadobutrol	1000mM	Bolus injection	1.5T 3D T1 weighted sequence	Not reported	2015 (Eide and Ringstad, 2015)
Rat	Isoflurane	Gd-DTPA, MW 938 Da	21 mM Gd-DTPA	80 μl 1.6μl/min	7.0T 3D T1-weighted FLASH	0.125 × 0.1 25 × 0.125 mm = 0.002 mm^3	2017 (Jiang et al., 2016)
Rat	Dexmedetomidine/ Isoflurane	Gd-DTPA, MW 938 Da	12.5 mM Gd-DTPA	20 μl 1.7μl/min	9.4T 3D T1-weighted FLASH	0.12 × 0.12 × 0.13 mm = 0.002 mm^3	2017 (Benveniste, et al., 2017)
Human	N/A, Awake	Gadobutrol	1000mM gadobutrol	0.5 ml Bolus injection	3T sagittal 3D T1-weighted scans	1 × 1 × 1 mm = 1 mm^3	2017 (Ringstad, et al., 2017)
Mouse	Isoflurane; Ketamine/ Xylazine	Gd-DTPA, MW 938 Da	500mM DOTA-Gd (DOTAREM®)	1-3 μL 1μ/min	7.0T 3D T1-weighted FLASH	0.078 × 0.078 × 0.150 = 0.001 mm^3	2018 (Gakuba et al., 2018)
Rat	Dexmedetomidine + low dose Isoflurane	Gadoterate meglumine (DOTAREM)	13.5 mM	20 μL 1.5 μl/min	9.4T 3D T1-weighted FLASH	0.24 × 0.24 × 0.26 mm =0.015 mm^3	2018 (Lee, et al., 2018)
Human	N/A, Awake	Gadobutrol	1000mM	0.5 ml Bolus injection	3T sagittal 3D T1-weighted scan	1 × 1 × 0.5 mm = 0.5 mm^3	2018 (Ringstad et al., 2018)
Mouse	Ketamine/ Xylazine	Gadoteridol (68mM, osmotically adjusted)	68 mM	10 μL 0.5 μl/min	11.75 T 3D FLASH	0.1 × 0.1 × 0.1 mm = 0.001 mm^3	2018 (Mestre, et al., 2018)
Nonhuman primate	Isoflurane	Gadoteridol	2mM	1ml/min	1.5T T1-weighted	unclear	2018 (Ohno, et al., 2019)
Rat	Isoflurane/N_2O	Gd-DTPA	21.7 mM	1.17 μL/min 1.67 μL/min 2.92 μL/min	7.0T 3D T1-weighted FLASH	0.125 × 0.1 67 × 0.167 mm = 0.003 mm^3	2018 (Ding, et al., 2018)
Rat	Isoflurane	Gd-DTPA	21 mM	80 μl at 1.6 μl/min & 4	9.4 T	?	2019 (Hadjihambi et al., 2019)

Species	Anesthesia	Contrast agent/ molecular weight (MW)	Contrast concentration (mM)	Volume and infusion rate	Magnetic field & sequence	Spatial resolution (mm^3)	Year [Reference]
				µl at 0.4 µl/ min,			
Rat	Dexmedeto midine + low dose Isoflurane	Gadoterate meglumine (DOTAREM)	13.5 mM	20 µL 1.5 µL/min	9.4T VFA-SPGR sequence	0.24 × 0.24 × 0.26 mm (0.015 mm^3)	2019 (Mortensen, et al., 2019)
Rat	Dexmedeto midine + low dose Isoflurane	Gadoterate meglumine (DOTAREM)	13.5mM and 100mM	20 µl 1.5 µL/mi n	9.4T VFA-SPGR sequence	0.30 × 0.30 × 0.30 mm 0.15 × 0.15 × 0.15 mm	2020 (Koundal, et al., 2020)

Table 2:

Overview of knowledge gained from glymphatic transport by DCE-MRI

Species	Route of Contrast	Glymphatic Parameters Measured	Physiological State or Disease?	Knowledge Gained	References
Rat	Intracisternal	- Time-activity curve - Cluster analysis	Physiological	- Visualized the paraarterial CSF pathways and areas of CSF-ISF exchange - Tracer size affects its distribution in the brain	2013 (Iliff, et al., 2013)
Mouse	Intracisternal	Visualization of contrast distribution throughout the brain	Various vascular pathologies	Glymphatic impairment was evident following subarachnoid hemorrhage and ischemic stroke, but not after common carotid artery occlusion and intracerebral hemorrhage	2014 (Gaberel, et al., 2014)
Rat	Intralumbar	Flow kinetics	Physiological	Utilized optimal mass transfer (OMT) method to create a glymphatic flow model	2015 (Ratner et al., 2015)
Rat	Intracisternal	- Time-signal curve - Flow kinetics	Physiological	Glymphatic transport was affected by body position and was most efficient in the right lateral decubitus position	2015 (Lee, et al., 2015)
Human	Intralumbar	T1 signal intensities of ROIs	Intracranial hypotension caused by CSF leakage	Contrast-enhanced MRI may be a viable technique for glymphatic studies in humans	2015 (Eide and Ringstad, 2015)
Human	Intravenous	T2 signal intensities of ROIs	Physiological	Intravenous contrast can enter the perivascular spaces via the CSF	2017 (Naganawa et al., 2017)
Rat	Intracisternal	Flow kinetics	Physiological	Improved upon previous work (Ratner, et al., 2015) on an optimal mass transfer (OMT) method to model glymphatic flow	2017 (Ratner, et al., 2017)
Rat	Intracisternal	- Time-evolution curve - Residual intensity - Clearance rate - Cluster analysis	Type 2 diabetes mellitus	- Glymphatic transport was impaired in rats with type 2 diabetes mellitus - Increased retention of contrast in the hippocampus and hypothalamus of rats with type 2 diabetes mellitus	2017 (Jiang et al., 2017)
Nonhuman Primate	Intracisternal	- Visualization of contrast distribution throughout the brain - T1 signal intensities of ROIs	Subarachnoid hemorrhage	Subarachnoid hemorrhage significantly impaired circulation of CSF through the parenchyma	2017 (Goulay et al., 2017)
Human	Intralumbar	- Time-signal curve - Clearance rate - T1 signal intensities of ROIs	Idiopathic normal pressure hydrocephalus	- Distribution of contrast throughout the brain was slower in humans when compared to rats - Glymphatic transport was decreased in patients with idiopathic normal pressure hydrocephalus, possibly due to restricted arterial pulsation	2017 (Ringstad, et al., 2017)
Rat	Intracisternal	- Time-signal curve - Clearance rate	Physiological	Glymphatic transport was increased in rats anesthetized with lowdose isoflurane supplemented with dexmedetomidine when compared to rats anesthetized with only isoflurane	2017 (Benveniste, et al., 2017)

Species	Route of Contrast	Glymphatic Parameters Measured	Physiological State or Disease?	Knowledge Gained	References
Mouse	Intracisternal	- Visualization of contrast distribution throughout the brain - T1 signal intensities of ROIs	Physiological	First study to show that glymphatic transport was decreased with anesthesia when compared to the awake state, in contrast to most other studies.	2018 (Gakuba, et al., 2018)
Rat	Intracisternal	- Visualization of contrast distribution throughout the brain - T1 signal intensities of ROIs - Time-activity curve	Physiological	Introduction of a B1+ correction factor for more accurate T1/ contrast measurements	2018 (Lee, et al., 2018)
Human	Intralumbar	T1 signal intensities of ROIs	Various CSF disorders	- Contrast drains from the CSF into the cervical lymph nodes - Drainage from nasal lymphatics and perineural pathways may be less pronounced in humans compared to rats	2018 (Eide et al., 2018)
Human	Intralumbar	- Visualization of contrast distribution throughout the brain - Time-signal curve - Clearance rate - T1 signal intensities of ROIs	Idiopathic normal pressure hydrocephalus	Clearance, but not uptake, of contrast was decreased in patients with idiopathic normal pressure hydrocephalus	2018 (Ringstad, et al., 2018)
Rat	Intravenous	- Time-signal curve - T1 signal intensities of ROIs	Physiological	- Signal intensity in the fourth ventricle increased immediately after intravenous contrast injection, suggesting the CSF as a potential intermediary pathway for contrast in the blood to reach the brain - Time-of-day of contrast injections may affect brain contrast concentrations	2018 (Taoka et al., 2018)
Rat Mouse	Intracisternal	- Visualization of contrast distribution throughout the brain - T1 signal intensities of ROIs	Physiological	Both flow and efflux of CSF increases as newborn rats and mice mature into adults	2018 (Di Palma et al., 2018)
Mouse	Intracisternal	- Visualization of contrast distribution throughout the brain - T1 signal intensities of ROIs	AQP4 knockout	A meta-analysis of five studies (using both microscopy and DCEMRI) strongly reinforced the theory that AQP4 facilitates the influx of CSF into the parenchyma	2018 (Mestre, et al., 2018)
Rat	Intracisternal	- Time-evolution curve - T1 signal intensities of ROIs	Physiological	- Described the effect of various contrast infusion rates on distribution and clearance Higher infusion rates show quicker distribution of contrast, but with a higher risk of disturbing CSF flow 2018	(Ding, et al., 2018)
Rat	Intracisternal	- Visualization of contrast distribution throughout the brain - Time-signal curve	Physiological	Introduced a mathematical model of the glymphatic system using local, rather than global, input functions	2019 (Davoodi-Bojd, et al., 2019)
Nonhuman Primate	- Intracisternal - Intralumbar - Intraventricular	- Visualization of contrast distribution throughout the brain - Clearance rate	Physiological	Distribution and clearance of tracer varies between different contrast delivery methods, with acute cisterna magna injection achieving the quickest and most extensive coverage of the brain	2019 (Ohno, et al., 2019)

Species	Route of Contrast	Glymphatic Parameters Measured	Physiological State or Disease?	Knowledge Gained	References
Rat	Intracisternal	- Visualization of contrast distribution throughout the brain - Time-signal curve - T1 signal intensities of ROIs	Chronic liver disease with minimal hepatic encephalopathy	Both influx and clearance of contrast in the frontal brain was decreased in rats with chronic liver disease, possibly due to decreased expression of aquaporin-4 in this region	2019 (Hadjihambi, et al., 2019)
Mouse	Intracisternal	- Visualization of contrast distribution throughout the brain and spinal cord - T1 signal intensities of ROIs	Experimental autoimmune encephalomyelitis (multiple sclerosis model)	Parenchymal CSF circulation in the spinal cord, but not the brain, was decreased in mice with a model of multiple sclerosis, possibly due to leukocyte infiltration	2019 (Fournier et al., 2019)
Phantom	N/A	T2 signal intensities of ROIs	N/A	Increasing repetition time (TR) helped increase the signal intensity of low concentration contrast, suggesting that higher TR may be utilized to detect low contrast concentrations in certain locations and after extended durations	2019 (Kato et al., 2019)
Human	Intravenous	T2 signal intensities of ROIs	Blood-brain barrier damage	Contrast in the blood may enter the CSF by way of the choroid plexus, aqueous humour, and/or trigeminal nerve	2019 (Deike-Hofmann et al., 2019)
Human	Intralumbar	- Visualization of contrast distribution throughout the brain - Concentrationtime curve	Physiological	Quantified contrast concentration in the human brain over a period of 3 days	2019 (Watts, et al., 2019)
Human	Intralumbar	T1 signal intensities of ROIs	Physiological	Contrast injected into the spinal subarachnoid space accessed the visual pathways, suggesting the existence of an ocular glymphatic system	2019 (Jacobsen et al., 2019)
Rat	Intracisternal	- Visualization of contrast distribution throughout the brain -Timeconcentration curve -Flow kinetics	Spontaneous hypertension	- Developed a new compartmental model to analyze contrast influx and efflux - Glymphatic influx and efflux was reduced in adult spontaneously hypertensive rats	2019 (Mortensen, et al., 2019)
Human	Intralumbar	Time for contrast to reach level of the foramen magnum (spinal transit time)	Various CSF disorders	- Intrathecal contrast injection is safe in humans without allergies to contrast - Contrast in the spinal cord reached the intracranial CSF in 99 out of 100 patients	2019 (Edeklev et al., 2019)
Human	Intravenous	Visualization of T1 signal intensities	Ultrasound-induced blood-brain barrier damage	Introduced a method of transient local blood-brain barrier opening to facilitate contrast penetration from the blood into the brain, allowing for local noninvasive visualization of the glymphatic system	2019 (Meng et al., 2019)
Human	Intralumbar	T1 and T2 signal intensities of ROIs	Various neurological diseases	- Simultaneously imaged the brain, putative meningeal lymph vessels, and deep cervical lymph nodes in humans, allowing for visualization of the glymphatic clearance pathways - Showed that clearance through these pathways may be impaired with aging	2020 (Zhou et al., 2020)
Human	Intravenous	Visualization of contrast distribution along vessels/ sinuses	Physiological	The space under the pial sheath of cortical vessels may	2020 (Naganawa et al., 2020)

Species	Route of Contrast	Glymphatic Parameters Measured	Physiological State or Disease?	Knowledge Gained	References
				be connected with meningeal lymphatics	
Rat	Intraventricular	T1 signal intensities of ROIs	Physiological	- Intraventricular injection of contrast may be plausible in glymphatic imaging - The distribution of contrast was more widespread during the dark phase of a light-dark cycle	2020 (Cai et al., 2020)
Rat	Yes	- Visualization of contrast distribution throughout the brain - Flow kinetics	Spontaneous hypertension	- Applied a novel method to reveal the contributions of advective and diffusive forces to glymphatic transport - Solute flow speed was reduced in spontaneously hypertensive rats	2020 (Koundal, et al., 2020)
Human	Intralumbar	- Time-signal curve - T1 signal intensities of ROIs	Physiological	Established a physiological baseline of CSF contrast kinetics in various cortical and subcortical areas of the human brain	2020 (Dyke et al., 2020)
Rat	Intracisternal	- Time-evolution curve - T1 signal intensities of ROIs	Ischemic stroke	- During the acute phase, clearance of contrast was slower in the hemisphere ipsilateral to ischemia - During the subacute phase, contrast's time-to-peak was longer and its retention was increased ipsilateral to ischemia	2020 (Lin et al., 2020)
Mouse	Intracisternal	- Visualization of contrast distribution throughout the brain - T1 signal intensities of ROIs	Physiological	- Introduced a new method of glymphatic transport quantification and analysis - Contrast drains from the brain into the deep cervical and submandibular lymph nodes	2020 (Xue, et al., 2020)
Rat	Intracisternal	- Time-signal curves - T1 signal intensities of ROIs	AQP4 inhibition	- Inhibition of AQP4 led to decreased influx of contrast into the parenchyma	2020 (Takano and Yamada, 2020)
Rat	Intracisternal	- Visualization of contrast distribution throughout the brain - Time-signal curves - Flow kinetics	Mild traumatic brain injury	Both glymphatic influx and clearance was persistently impaired during the chronic time course following mild traumatic brain injury	2020 (Li et al., 2020)